Velocity renormalization and Dirac cone multiplication in graphene superlattices with various barrier-edge geometries

A. de Jamblinne de Meux,[1] N. Leconte,[1,2] J.-C. Charlier,[1] and A. Lherbier[1]

[1]*Institute of Condensed Matter and Nanosciences (IMCN), Université catholique de Louvain (UCL),*
Chemin des étoiles 8, B-1348 Louvain-la-Neuve, Belgium

[2]*ICN2 - Institut Catala de Nanociencia i Nanotecnologia, Campus UAB, 08193 Bellaterra (Barcelona), Spain*

The electronic properties of one-dimensional graphene superlattices strongly depend on the atomic size and orientation of the 1D external periodic potential. Using a tight-binding approach, we show that the armchair and zigzag directions in these superlattices have a different impact on the renormalization of the anisotropic velocity of the charge carriers. For symmetric potential barriers, the velocity perpendicular to the barrier is modified for the armchair direction while remaining unchanged in the zigzag case. For asymmetric barriers, the initial symmetry between the forward and backward momentum with respect to the Dirac cone symmetry is broken for the velocity perpendicular (armchair case) or parallel (zigzag case) to the barriers. At last, Dirac cone multiplication at the charge neutrality point occurs only for the zigzag geometry. In contrast, band gaps appear in the electronic structure of the graphene superlattice with barrier in the armchair direction.

I. INTRODUCTION

Graphene has attracted much attention since 2004 [1] with the first experimental characterizations unveiling its amazing electronic and transport properties [2]. The unique behavior of massless chiral electrons present in graphene gives rise to uncommon effects such as the minimum of conductivity [3], Klein tunneling [4] of charge carriers, and the anomalous quantum Hall effect [5]. Such tremendous properties related to pseudorelativistic effects have motivated intense efforts towards the realization of graphene-based electronics [6–10].

Within the variety of graphene-based devices for which a great potential is foreseen, the specificities of graphene superlattices have triggered special interest [11–22]. In particular, one-dimensional (1D) graphene superlattices (SLs), which can be obtained by controlled surface patterning, might exhibit electron beam supercollimation [23]. Furthermore, the possibility of creating new Dirac cones at the charge neutrality point (CNP) or at low excitation energy is also an interesting feature of graphene SLs, both in single and bi-layer graphene [24]. The appearance of new Dirac cones corresponds to observable dips in the density of state (DOS), which were observed experimentally by STM measurements on graphene exposed to a Moiré pattern [25–29] and in corrugated graphene [30]. 1D SLs can serve as simplified models for both corrugated graphene and graphene modulated by an external electrical field.

The directional dependency of the electron propagation in 1D graphene SLs is related to an unexpected anisotropy of the electron velocity. In the direction perpendicular to the potential barrier, the velocity of the electron remains constant and is always equal to the velocity of pristine graphene. This behavior is unaffected by the width W, the height U, or the modulation period L of the barrier. In sharp contrast, the velocity parallel to the barrier is strongly impacted by these three parameters. In certain cases, the velocity in the direction parallel to the barrier can even completely vanish [11,12]. Further experimental work confirmed and extended these first observations. In particular, Dubey *et al.* [31] succeeded to

fabricate 1D SLs and observed the variation of the resistance of this structure as a function of the barrier height. Their observations corroborate the appearance of new Dirac cones at the charge neutrality points predicted by Barber *et al.* [32] and Ho *et al.* [33]. Including the influence of the barriers edges, Lee *et al.* [34] showed by *ab initio* calculation that gaps can appear in 1D SLs with barriers in the armchair direction, while this is not the case in the zigzag direction. In the experimental part, the graphene samples were suspended over periodic nanotrenches patterned in the substrate. Since interaction with the substrate is believed to introduce chemical doping through the adsorption of oxygen, the periodic potential was modeled by epoxy oxygens adatoms, which can lead to impurity specific physics, such as resonant states leading to localization effects [35]. It is therefore not clear if the apparition of those gaps is due to the oxygen adatoms or due to the presence of the SL.

The first results by Lee *et al.* [34] and the known importance of edge physics in graphene ribbons [36,37] call for a more systematic analysis, taking into account the effect of edge physics of the barriers in 1D SLs. The experimental realization of controlled 1D SLs is possible, albeit a challenging task. If the chiral directions of a graphene sheet are known, alignment of periodic gates on a patterned surface is possible. As an example, Ponomarenko *et al.* successfully align graphene on hexagonal boron nitride [26]. The knowledge of the chirality is more challenging. A first possibility is through CVD grown graphene, which was reported to exhibit hexagonally shaped grains with aligned edges, mostly, in the zigzag direction [38]. Another solution would be to etch a small portion of the graphene via iron catalysts [39]. As the chirality along the etched line is preserved, alignment becomes possible in this direction.

In this paper, the differences between the zigzag SLs (ZSLs) and armchair SLs (ASLs) are investigated systematically by comparing the impact of the three relevant parameters defining a 1D SL: U, W, and L. The following conclusions are drawn. By taking into account the different orientations of the 1D SL (zigzag and armchair), the Dirac cone multiplication behavior

is complexified. The energy position of the additional Dirac cones depends on the value of U, as predicted by Park *et al.* [11]. In addition, the new cones at the charge neutrality point (CNP) described by Ho *et al.* [33] only appear for ZSLs and lead to the apparition of three families of cones. In contrast, for ASLs, band gaps appear in the density of states. Depending on the number of carbon dimers making up the barrier, ASLs can be classified into three families. Finally, the velocity modulation quantified by Barbier *et al.* [32] is also impacted by the SL barrier edge geometry. For symmetric barriers, the velocity perpendicular to the barriers is modified for ASLs and is robust in the case of ZSLs. For asymmetric barriers, velocity renormalization is observed in both directions for all SLs. These asymmetric barriers also break the initial symmetry between the forward and backward momentum direction for one of the two main directions of the velocity: in the perpendicular direction for ASLs and in the parallel direction for ZSLs.

This systematic analysis is organized into three different sections in this paper, namely the impact of the parameters defining the barrier on the DOS and the band structure (Sec. III), on the velocity at the CNP (Sec. IV), and finally, on the velocity at higher energies (Sec. V). The numerical techniques and the model used to describe the SLs are presented in Sec. II. Section VI describes the effect of white noise disorder on our calculations.

II. NUMERICAL TECHNIQUES AND MODEL

The Hamiltonian is expressed in an orthogonal single p_z orbital basis set. The tight-binding model accounts only for first nearest-neighbor interactions described by the hopping term $\gamma_0 = -2.6$ eV. The Hamiltonian of the two-dimensional periodic system reads as

$$H = \epsilon_z \sum_i c_i^\dagger c_i + \gamma_0 \sum_{\langle i,j \rangle} c_i^\dagger c_j, \tag{1}$$

where $c_i^\dagger$ and c_i are creator and annihilator operators on atomic site i and where $\langle i,j \rangle$ denotes that the sum runs only on the atomic site j denoting the first nearest neighbors of atomic site i. The on-site energy term ϵ_z accounts for the local electrostatic environment.

To create a 1D periodic superlattice potential on top of the 2D graphene plane, two electrostatic regions can be defined by setting ϵ_z to ϵ_1 or ϵ_2 depending on whether the atomic site belongs to the first or the second electrostatic region. No other modifications than the onsite terms of the Hamiltonian are performed to account for the presence of the electrostatic barrier potential. In particular, the hopping terms between atomic sites belonging to the two separate regions remain unchanged (i.e., equal to γ_0). While cutting graphene into nanoribbons will produce physical edges, here, the system remains an infinite 2D graphene plane but with a 1D periodic potential imposing a given 1D orientation with respect to the crystal.

Figure 1 depicts how ZSLs and ASLs are modeled. Their structures are composed of two potential barriers of widths W_1 and W_2 repeated periodically with period $L = W_1 + W_2$. The barrier heights are given by ϵ_1 and ϵ_2, respectively.
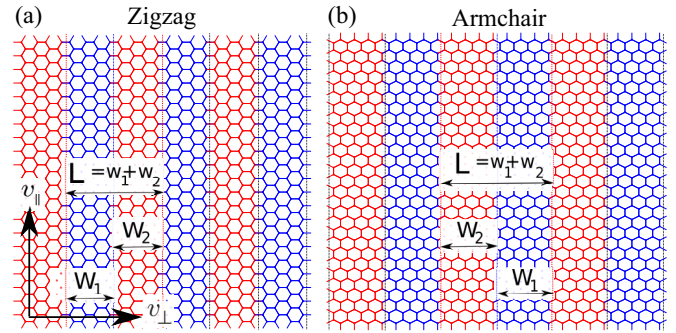

FIG. 1. (Color online) Representation of graphene SLs with the potential applied in (a) the zigzag direction and (b) the armchair direction. The blue regions contain atoms with an applied potential ϵ_1 that form potential barriers of width W_1. The red regions form barriers of width W_2 and contain atoms with applied potential ϵ_2. L is the periodicity of the pattern.

Actually, only the potential difference $U = \epsilon_1 - \epsilon_2$ induces a modification of the electronic properties discussed in this paper, notwithstanding a rigid shift of the CNP, which is given by

$$\frac{W_1\epsilon_1 + W_2\epsilon_2}{L}. \tag{2}$$

It is therefore easier to work with an effective potential U by setting $\epsilon_1 = 0$ eV and $\epsilon_2 = U$, and to realign *a posteriori* the CNP to zero energy in order to compare the different systems. Only moderate values of U are considered, as larger values are not achievable experimentally and because the model becomes unreliable for large values of U. Finally, in this paper, $W = W_2$ and, unless stated otherwise, $W_2 = L/2$ (symmetric barrier).

The presence of a 1D periodic potential, creating a regular superlattice, maintains the transport in the ballistic regime, i.e., the propagation is governed by periodic extended Bloch states. Therefore in such perfect SLs, the only relevant quantities governing the ballistic transport are the DOS and the carrier velocities. The velocity can be evaluated from the electronic band structure computed by a direct diagonalization of the Hamiltonian around a given k point:

$$v_k = \frac{1}{\hbar}\frac{\partial E(k)}{\partial k}. \tag{3}$$

The energy dependency of the velocity $v(E)$ can then be computed by integrating over the whole Brillouin zone. Alternatively, the real-space TB-based Kubo-Greenwood formalism, as described in Refs. [35,40–46], can be used to compute carrier velocities from the spreading of wave packets in the ballistic regime. Unfortunately, for graphene, the velocity cannot be accurately computed at the CNP in this formalism because a mathematical singularity exists at this point (see Appendix for more information). The other transport quantities such as the semi-classical conductivity, the mean free path or the mobility, typically accessible within the Kubo-Greenwood approach, are only well defined in the diffusive regime. This regime is, however, only obtained after multiple scattering events in the presence of a stochastic disorder potential. The Kubo-Greenwood method can also describe quantum localization effects in disordered systems. The present paper

mainly focuses on perfect systems, where charge carriers remain in the ballistic regime for the whole energy spectrum. The impact of disorder is discussed in Sec. VI at the end of the paper.

Finally, the DOS can be calculated independently of the time evolution of wave packets thanks to the Haydock recursion method using a Lanczos algorithm with continued fraction calculations [47].

III. DENSITY OF STATES AND ELECTRONIC BAND STRUCTURE

A. Generic characteristics for ASLs and ZSLs

The main impact of an SL on the DOS is the presence of the local dips corresponding to the apparition of new Dirac cones. The energy position of these dips in the calculated DOS presented in Fig. 2 using $U = 1.04$ eV (red dots for ASL and blue line for ZSL) is in agreement with the following analytical formula (vertical dashed lines) given by Park *et al.* [12] up to $E = 1$ eV, which confirms that the position of the new Dirac cones only depends on L:

$$E_m = \pm \hbar v_F \frac{m\pi}{L}, \qquad (4)$$

with v_F the Fermi velocity in pristine graphene and m an integer. At higher energies, the agreement between numerics and analytics becomes gradually worse, but this is not relevant because the simplified first neighbor TB model

loses its pertinence there and because such energies are in principle experimentally inaccessible to electronic transport measurements.

In the DOS, each dip associated to a Dirac cone is preceded by a peak due to secondary van Hove singularities (VHS) in the electronic band structure. The amplitude of these VHS is influenced by the potential U. For small values of U, the dips and associated secondary VHS are not visible in the DOS although Dirac cones can be identified in the electronic band structure (not shown here).

For values of W different from the symmetric case (i.e., $W \neq L/2$), an electron-hole asymmetry in the DOS is created, and the amplitudes of the secondary VHS change. Nevertheless, the energy position of the peaks is robust to this change of W. For a given L, the DOS curves corresponding to SLs given by widths W and $|L/2 - W|$ are antisymmetric to each other around the CNP [see panels (b) and (c) of Fig. 2]

B. Superlattice barrier edge-dependent characteristics

For sufficiently large values of U and small values of L, a splitting of the secondary VHS occurs for ZSLs. This splitting is not observed for ASLs, as depicted in Fig. 2(a). In addition, for ASLs, band gaps can appear under certain conditions (see Figs. 3–5). Their existence depends on the number of carbon dimers $3p + n$ (with $n = 0, 1$, or 2 and p an integer) in the barrier, which allows to group the ASLs into three families defined by the value of n (see inset of Fig. 4 for visual representation of the dimers). At low potential (for $U \gtrsim 0$), a gap only opens up for the family where $n = 0$. Higher values of potential ($U \gg 0$) are required to observe gaps for the two other families ($n = 1, 2$). The values of the gaps are generally very small (few meV) as illustrated in Fig. 3, and are inversely
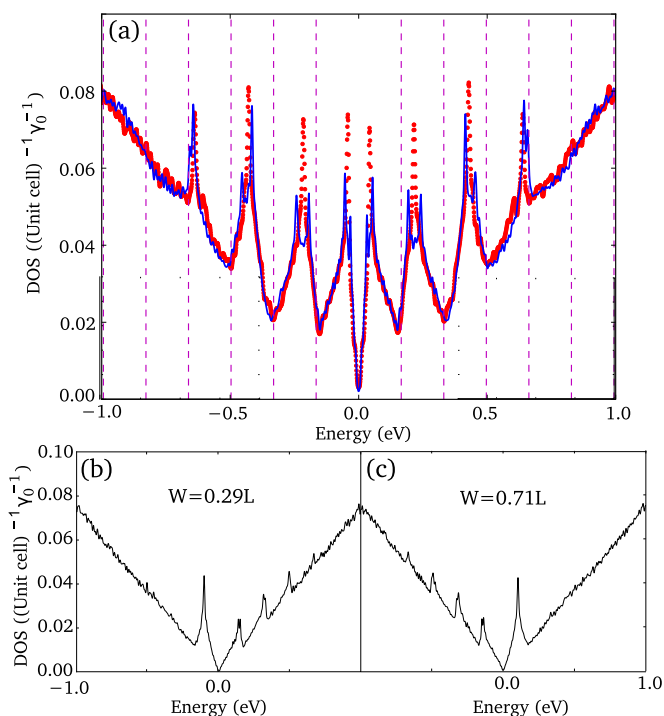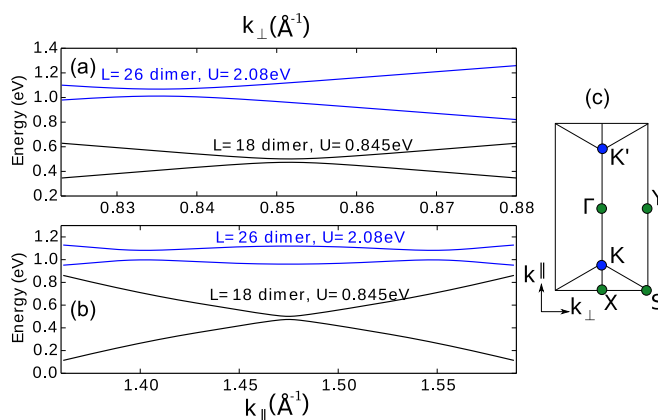

FIG. 2. (Color online) DOS of SLs. (a) Difference between the DOS for a ASL (dotted red points) and ZSL (solid blue line). Both DOS are given for a potential $U = 1.04$ eV and a period L of 10 nm. The dashed vertical line gives the position of the new Dirac cones as given by Eq. (4). The only visible difference is the splitting of the peaks for ZSL. Antisymmetric DOS around the CNP for ZSLs with $W = 0.29L$ (b) and $W = 0.71L$ (c) ($L = 10$ nm, $U = 0.52$ eV).

FIG. 3. (Color online) Band structure close to the K point for two ASLs ($U = 0.845$ and $U = 2.08$, depicted in black and blue, respectively) with band gap in the $k_\perp$ (a) and $k_\parallel$ (b) directions. The CNP was not realigned at $E = 0$ for this figure. As expected, its position is given by $U/2$ (because $L = W/2$ in Eq. 2). (c) Brillouin zone (BZ) associated to the unit cell, the position of the Dirac cone (if it exists) is labeled K in reference to its position in the original hexagonal BZ of graphene. For ASLs, if multiple cones do not appear, the conduction and valance bands still present multiple maxima and minima in the $k_\parallel$ direction when L and U are large enough [e.g., (b), blue case].
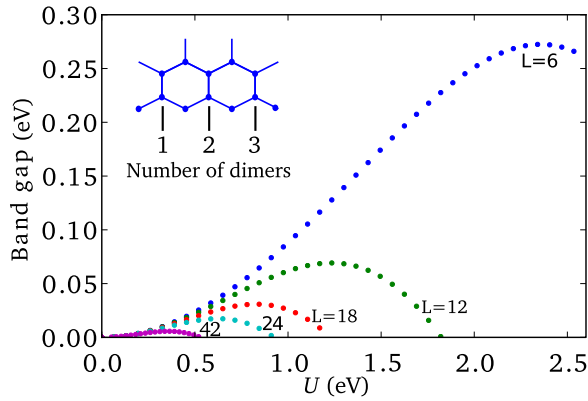
FIG. 4. (Color online) Variation of the gap with U for different ASLs. The value of W ($=L/2$) is chosen so that all the SLs are from the $3p$ family ($n = 0$). The value of L is given in number of dimers as described by the inset.

proportional to W. The exact value of the gap can then be fine-tuned by varying U following the bell shape as pictured in Fig. 4. The DOS corresponding to the largest calculated band gap is shown in Fig. 5.

IV. VELOCITY AT THE CHARGE NEUTRALITY POINT

Focusing on the central dip in the DOS, i.e., at the CNP, the multiplication of cones at this energy observed by Ho *et al.* [33] only occurs for ZSLs for which $W = L/2$. The present simulations agree with the creation-by-pairs model developed by Barbier *et al.* [32]. Nevertheless, our simulations indicate that these new cones can be classified into two categories, each with different properties from the original cone (labeled *main* Dirac cone in the rest of this paper). If $W \neq L/2$, these new cones are shifted in energy away from the CNP (positioned at zero energy by convention). This behavior is discussed in Sec. V focusing on the energy dependency of the velocity. Large variations of W from the symmetric case
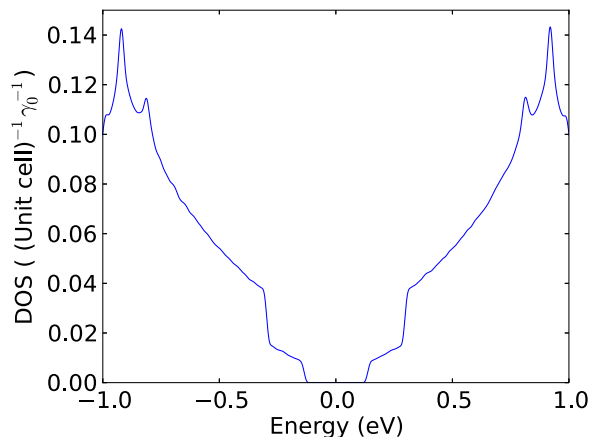

FIG. 5. (Color online) Density of states for the ASLs having the largest gap in Fig. 4 (i.e., L containing six dimers and $U = 2.34$ eV). The gap is clearly visible and has the same value as the one obtained directly from the band structure, confirming the existence of the observed gaps.

($W = L/2$) reduce the number of cones. In other words, if W tends to L or 0 all the new cones disappear. The present section focuses solely on the symmetric configuration ($W = L/2$) where all the new cones appearing in ZSLs are at the CNP.

A. Symmetric ZSLs

As predicted by Park *et al.* [11], SLs induce an anisotropic velocity renormalization. This picture is depicted and extended in Fig. 6. The velocities are described as a function of U. Because the determining factor for this velocity renormalization is actually the product LU, similar curves (not shown here) can be obtained by varying L and keeping U constant. This comment is valid for the remaining of the section.

In Fig. 6, the *main* Dirac cone at the CNP (blue circle symbol) has the same flavor as the one described by Park *et al.* [11], namely, that the velocity perpendicular to the barrier, $v_\perp^m$ (m for *main*) in panel (a), is constant and equals the velocity in pristine graphene, while the velocity parallel to the barrier, $v_\parallel^m$ in panel (b), varies periodically and goes to zero for certain values of U. New cones appear at the CNP for symmetric barriers. All the cones generated on the *left* side of the *main* cone in panel (c) (plus, minus and triangle symbols) are part of a second flavor. The third flavor contains the cones created on the *right* side (diamond, cross and star symbols) of the *main* cone.

Apart from the two first new cones (plus and star symbols), each set of two new cones appears slightly before the minimum of $v_\parallel^m$ [see, for instance, diamond and triangle symbols in Fig. 6(c)]. The energy difference between this minimum and the energy at which the new cones appear increases with U or L.

Cones of second and third flavor roughly depict a similar behavior for the velocity renormalization with U (or L). Indeed, $v_\parallel$ always starts from zero and slowly saturates with U (L). Surprisingly, the velocity for the last cone (star symbols) is higher than the velocity for pristine graphene. The reason for it contrasts with the squeezing of the Dirac cone due to electron-electron interactions [48]. A difference in behavior between the *left* and *right* cones is also visible: the velocity of the *left* cones saturates more quickly than the velocity of the *right* cones.

In the perpendicular direction, all characteristics are inverted: the velocity goes from the velocity of pristine graphene toward zero and decreases more quickly for the cones on the *right*. Barber *et al.* [32] found a similar behavior for the additional cones. Nevertheless, this separation into two classes, with slightly different properties, was missing in their analysis. They also found that the new cones appear at a minimum of $v_\parallel^m$, a conclusion which is slightly modified here.

For the velocities calculated at directions in between the perpendicular and the parallel one, the velocities $v_\perp$ and $v_\parallel$ always appear for all families as extrema and the velocity changes smoothly between them.

B. Symmetric ASLs

For ASLs, the impact of the parameters L and U is not completely captured by the product LU because of the existence of three families. When U does not allow to switch
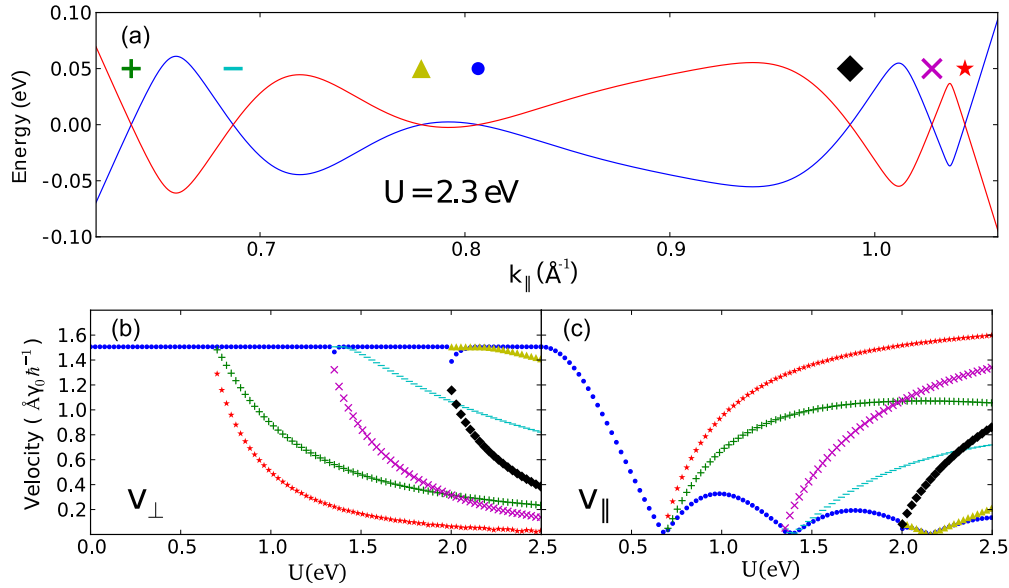
FIG. 6. (Color online) Variation of the velocity at the CNP in the directions perpendicular ($\perp$) (b) and parallel ($\parallel$) (c) to the potential barrier, for ZSLs. Each symbol in (b) and (c) is associated to a particular cone as depicted in panel (a) representing the band structure for a chosen potential, $U = 2.3$ eV, in the direction $k_{\parallel}$. $L = 10$ nm and $W = L/2$. The *main* (or original) cone is always at the center and its velocity is depicted by the blue circles. The new cones appear two by two, one on each side of the *main* cone. The last cones to appear are therefore closest to the *main* cone. Corresponding symbols between (a)–(c) are used to facilitate reading.

between those families, the value of L can, and this will thus induce a different behavior.

Figure 7 shows the velocity renormalization for the ASLs case (for $W = L/2$) when changing the value of L and Fig. 8 when the value of U is modified. For the renormalization in the function of L, all data points are gathered in Fig. 7(a) but also separated into the three families $n = 0$, 1, or 2 in the

panels (b), (c), and (d), according to the previous discussion in Sec. III B. After separation into three families, the similarities between the variation of U and L are recovered [compare Figs. 7(b), 7(c), 7(d) and Figs. 8(a), 8(b), 8(c), respectively]. The overall behavior of $v_{\perp}$ is similar as the one of ZSLs, provided the values of U or L that create a band gap are excluded (inducing an absence of velocity at the CNP). Since Dirac cone multiplication does not occur for this barrier edge geometry, only the velocity of the main Dirac cone is depicted
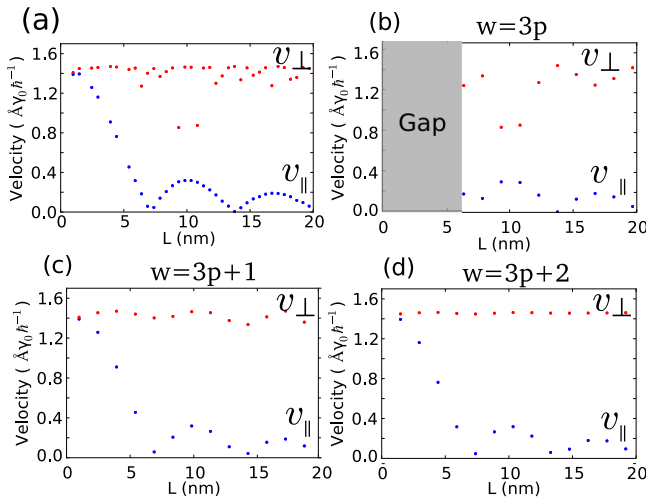

FIG. 7. (Color online) Variation of the velocity with L at the CNP for symmetric ASLs for the three families : $3p$, $3p + 1$, and $3p + 2$, with $W = L/2$ and $U = 1$ eV. (a) The data points obtained without distinction between the families of ASLs depict nonmonotonous variations in the velocity in the $\perp$ direction. Separating into the three families (b), (c), and (d), the curves make more sense for this direction. In the $\parallel$ direction, the velocity is completely similar to what is observed with ZSLs.
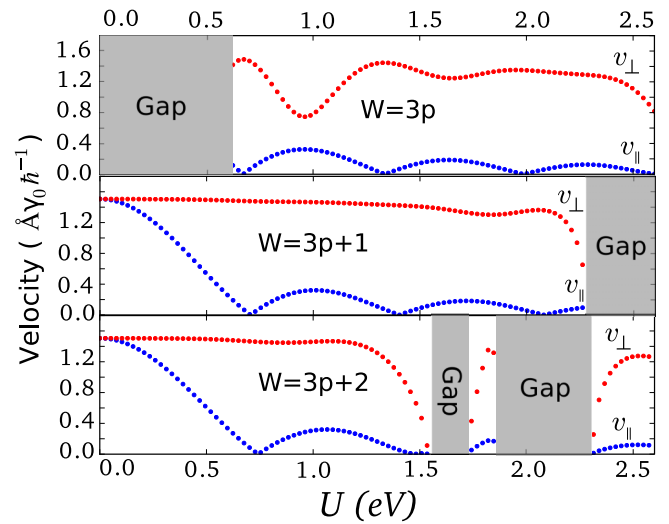

FIG. 8. (Color online) Variation of the velocity with U at the CNP for symmetric ASLs for the three families: $3p$, $3p + 1$, and $3p + 2$. The period L used is 21, 19, and 20 dimers, respectively. The shaded area highlights the position of the gaps. Only the $3p$ family has a gap at low potential. Near a gap, the oscillations of $v_{\perp}$ increase up to a point where the velocity falls rapidly to zero.
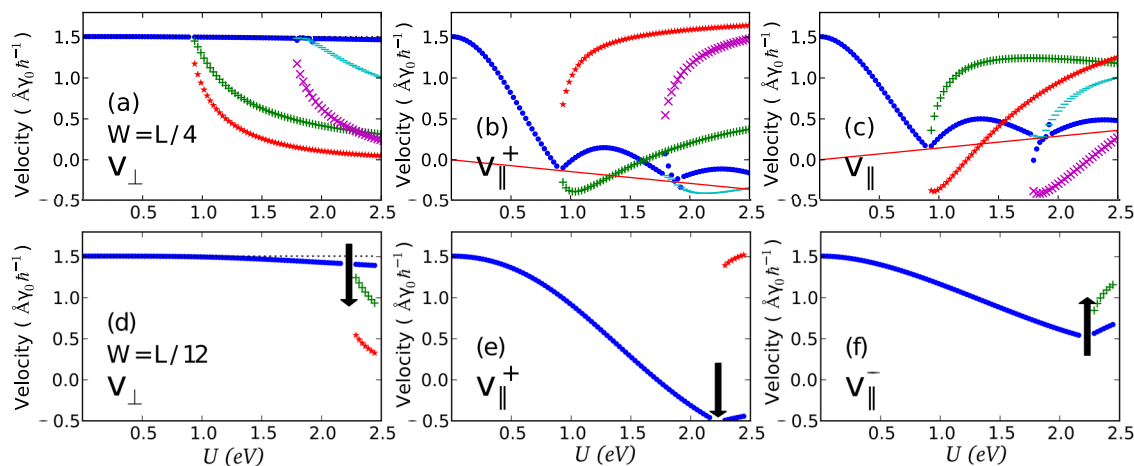
FIG. 9. (Color online) Variations of the velocity with U for asymmetric ZSLs, $L = 48$ dimers (~ 10 nm). The correspondence of the symbols is the same as the one used in Fig. 6. [(a), (b), and (c)] $W = L/4 = 12$ dimers. [(d), (e), and (f)] $W = L/12 = 4$ dimers. When W goes towards 0 (L), the asymmetry between $v_{\parallel}^-$ and $v_{\parallel}^+$ increases. The black arrows in (d), (e), and (f) indicate the direction of the curve when varying W towards zero. The reduction is nonlinear and increases when W is closest to 0. Similarly, the U dependency of the curves is also dilated when W decreases (transition between upper and lower panels). At the limit $W = 0$, the dilation would become infinite, recovering the properties of pristine graphene.

for ASLs. For $v_{\parallel}$, the behavior is similar to ZSLs [compare for instance blue circle symbols in Figs. 6(c) and 7(a) (or Fig. 8)], which confirms the L and U-dependency highlighted above. For $v_{\perp}$, the behavior is different than for ZSLs. Indeed, this velocity now varies, in contrast to the constant value observed for ZSLs [Fig. 6(b)]. As displayed in Fig. 7, these variations depend on the family to which the ASLs belongs to ($n = 0, 1$ or 2), which explains the nonmonotonous variations in the velocity observed. When approaching the gaps, oscillations of the otherwise constant value of $v_{\perp}$ are observed. The perpendicular velocity eventually vanishes when the gap region is reached (see Fig. 8).

C. Asymmetric ZSLs

An asymmetry between the modified and pristine zone ($W \neq L/2$) has also a large impact on the velocity renormalization. The effect at the CNP is larger for ZSLs. Because of the asymmetry, the new Dirac cones are not generated at the CNP anymore (and those will thus be discussed in the next section). In this paragraph, only the impact on the *main* cone (blue circle symbols in Fig. 9) is considered.

The first effect of this asymmetry in ZSLs is to break the equivalence between the $k_{\parallel}^+$ and $k_{\parallel}^-$ direction for $v_{\parallel}$ (see Fig. 12 for sign convention). This difference in the behavior of velocities $v_{\parallel}^+$ and $-v_{\parallel}^-$ is illustrated in Fig. 9.

The blue circles in Figs. 9(b) and 9(c) suggest that, for a given valley K, some asymmetry is obtained depending on the direction of the carrier flow through the barrier for $U \geqslant 1$ eV. Nevertheless, a correspondence exists between the two velocities. The velocity $v_{\parallel}^+ (-v_{\parallel}^-)$ obtained for a width W is exactly the same as the velocity $-v_{\parallel}^- (v_{\parallel}^+)$ obtained for a width $L - W$, respectively.

Looking at the impact of U, both $v_{\parallel}$ and $v_{\perp}$ are affected, in opposition to the symmetric case. $v_{\perp}$ now presents a decreasing behavior with U, which gets more pronounced when W

tends towards L or 0 and completely disappears at $W = L/2$, consistent with previous observations.

In Fig. 9(a), for $W = L/4$, the decrease is not very pronounced in comparison with the (constant) dotted line found for $W = L/2$. As W decreases further, the renormalization of $v_{\perp}$ gets more pronounced [see panel (d)]. The effect of U has a larger impact on $v_{\parallel}$ [panels (b) and (c)]. First, the minima of $v_{\parallel}$ are not any more at zero. Then, the behavior of $v_{\parallel}^-$ and $v_{\parallel}^+$ is opposite: if the value of the minima increases for $-v_{\parallel}^-$ [as in panels (c) and (f)], the value of the minima in $v_{\parallel}^+$ decreases [as in panels (b) and (e)]. In a first approximation, if W is not too small, the minima are aligned on the red line starting from zero [panels (b) and (c)]. The slope of this line is opposite for $v_{\parallel}^+$ and $-v_{\parallel}^-$ and decreases when W goes to $L/2$, eventually recovering the behavior of the symmetric barriers, where both velocity directions are degenerated. However, if W is small (a few percent of the value of L), the line joining the minima does not cross the origin of the plot [i.e., (0,0)] anymore, and is different for both directions (not shown here). In such case, the larger the velocity renormalization is in one direction (take for instance $v_{\parallel}^-$), the smaller it is in the opposite direction ($v_{\parallel}^+$), as is already visible by comparing panels (e) and (f).

Finally, by varying W (see the green dots corresponding to the main cone in Fig. 10), the impact of asymmetric barriers becomes apparent as well. In this situation, Figs. 10(b) and 10(c) can be obtained from one another by central symmetry around the point ($v = 0, W = L/2$) (as already mentioned at the beginning of this paragraph). The other curves in this figure (blue and red dots in Fig. 10) are left for Sec. V, where the velocities away from the CNP are discussed.

D. Asymmetric ASLs

For ASLs, the asymmetry induced by the value of W, has a weaker influence on the velocity renormalization, in comparison with ZSLs. The values of $v_{\parallel}$ stay symmetric (i.e.,
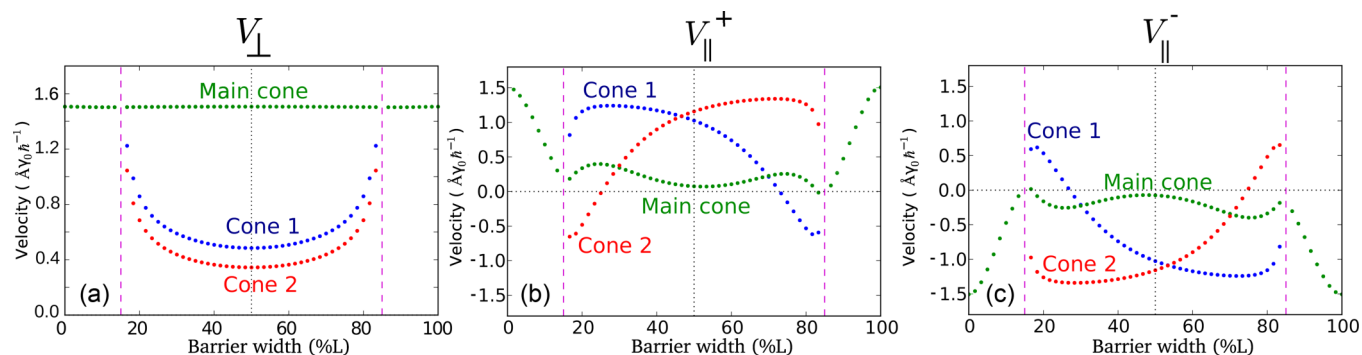
FIG. 10. (Color online) Variations of the velocity with the barrier width when several cones are present for ZSLs. $L = 120$ dimers ($\sim$26 nm). A large value of L is used to have more points in the curve. Indeed, an integer number of dimers for W and L is required. Therefore, the larger the value of L, the larger the number of points that can be computed. $U = 0.52$ eV. (a) The velocity in the $\perp$ direction is constant for the *main* cone and varies from the velocity of pristine graphene to a minimum situated at $W = L/2$ for the other cones. (b) and (c) represent the values of the velocity in the two inequivalent branches of the cones for the parallel direction. Additional cones are only found in the central zone with an L between $\sim$16% and $\sim$84%. The variations of the velocities of the two new cones are opposite. Contrary to the main cone, an inversion of the velocity is observed for the new cones. Results obtained for smaller values of L are similar.

no degeneracy lifting between $v_\parallel^+$ and $v_\parallel^-$) for $W \leqslant L/2$ and the dependency on the U parameter is similar to the one observed for $W = L/2$. In contrast, the degeneracy is lifted for $v_\perp$, albeit quite softly. More specifically, the oscillations in the vicinity of the band gaps are different, as depicted in Fig. 11 for the $3p + 1$ family (for the position of the band gaps for different families, see Fig. 8).

V. ENERGY DEPENDENCY OF THE VELOCITY

As mentioned previously, the periodic potential does not only modify the velocity at the CNP, but also impacts the velocity at higher energies. Those energies are the topic of this section. On the one hand (Sec. V A), for energies close to the CNP ($\leqslant$0.1 eV), only the asymmetric ZSLs ($W \neq L/2$) are discussed, for which the new cones shift away from the CNP. ASLs do not induce additional cones, and are thus excluded from this discussion. On the other hand (Sec. V B), at higher energies ($\gg$0.1 eV), the differences between ASLs and ZSLs disappear. The focus is thus shifted towards the velocities at intermediate incident angles.
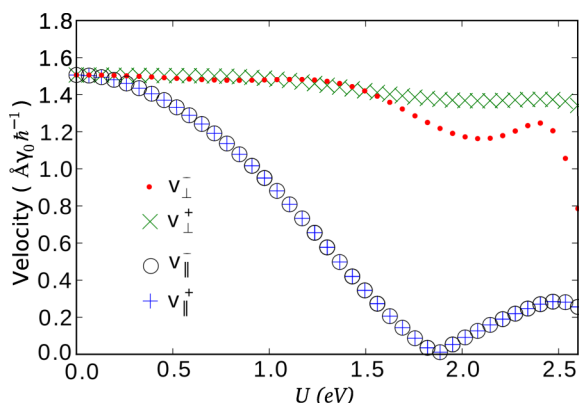

FIG. 11. (Color online) Variations of the velocity with U for asymmetric ASLs. $L = 40$ dimers ($\sim$10 nm) and $W = L/10 = 4(3p + 1$ family). No anisotropy exists for $v_\parallel^-$. In opposition to ZSLs, $v_\perp$ exhibits an anisotropy between the $+$ and $-$ directions.

A. Asymmetric ZSLs

Going back to Fig. 9, showing the impact of the asymmetry on the additional cones (plus, minus, cross, and star symbols) as a function of U, the inequivalence between $k_\parallel^+$ and $k_\parallel^-$ directions is clearly apparent, as it was already observed for the *main* cone (blue circles).

Varying now the parameter W (Fig. 10), two zones can be distinguished (separated by dashed vertical purple lines). In the first zone (outer region, where W is close to 0 or L), the value of $|L - W|$ is too small to create multiple cones (only the main cone exists). A simple renormalization of the velocity parallel to the barrier ($v_\parallel^-$), similar to the one occurring by changing the U parameter, is observed. In the second zone (central region), the velocities corresponding to the additional cones show a more exotic behavior. In particular, close to the boundary between the two zones, the velocities of the additional cones have the same sign in $v_\parallel^+$ and $v_\parallel^-$. This is somehow unusual because it means that the slopes of the two bands forming the cone in the $\parallel$ direction have the same sign. This curious behavior of the additional cones can be visualized by looking at the evolution of the band structure as a function of W in Fig. 12. For $W = L/5$ [panel (a)], the cones are tilted in such a way that the velocities have the same sign (upper insets zoom in on this peculiar behavior). For higher values of W/L (here at 26.6%), one of the branches becomes parallel to the $k_\parallel$ axis and thus the velocity drops to zero [see panel (b)]. After this transition value, a situation occurs where the velocities in the cone have opposite signs [see panel (c)]. The absolute values of these velocities are not yet equal because the cone is still slightly rotated. By increasing further the value of W, the velocities become closer and closer to each other in absolute value, to finally recover the symmetric barriers case discussed in previous sections.

B. Angle dependency

Up to now, only the 0° ($\perp$) and the 90° ($\parallel$) cases have been discussed, being the most straightforward. We found that the velocity changes smoothly between these two extreme cases. The present section extends the analysis for these intermediate
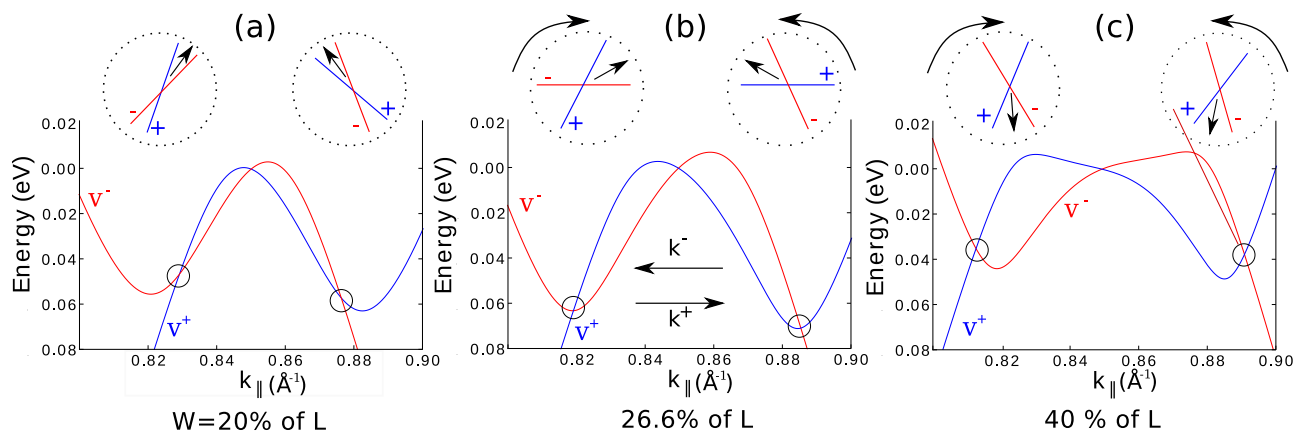
FIG. 12. (Color online) Rotation of the Dirac cones with the modification of W for ZSLs. The arrows outside the circle above the graph indicate the fictive rotation direction when transitioning the values of W from (a) to (c). The arrow inside the cone has no physical meaning, but helps visualize the cone rotation. v^+ and v^- are defined as the velocities on the two branches of the cones. The corresponding branches are color-coded in the main frames below. v^- is taken on the branch showing an overall decreasing behavior and v^+ an overall increasing behavior. (a) Both branches of the cone have the same slope: v^- and v^+ have the same sign. (b) One of the bands is flat: v^- or v^+ is zero. (c) The two branches have opposite slopes but the cone is still slightly turned: v^- and v^+ have opposite signs but different values.

angles at energies away from the CNP, leading to richer physics. For this analysis the velocities are computed within the Kubo-Greenwood method in the ballistic regime. ZSLs and ASLs behave very similarly at higher energies. Therefore, only ZSLs are depicted.

In Fig. 13, both the angle and the energy dependence are clearly visible. At the CNP, the evaluation of velocity is hindered by numerical divergences (shaded region in Fig. 13), difficult to resolve using the diagonalization trick, because of the angle dependency. For energies very close to the CNP, the low-angle velocity (close to $0° \equiv v_\perp$) is larger than the high-angle velocity (close to $90° \equiv v_\parallel$). For higher energies, i.e., away from the CNP, the behavior is inverted. The transition

between these two regimes occurs around 0.12 eV in Fig. 13, which corresponds to the position of the first peak (VHS) in the DOS.

For even higher energies, periodic oscillations in the velocity appear. The amplitude of these oscillations is maximum for smallest angles ($v_\perp$) and becomes barely noticeable for largest angles. Every minimum of the velocity corresponds to the position of a Dirac cone in the electronic band structure, which corresponds also to a minimum in the DOS. Even if the minima are not apparent in the DOS (see Fig. 2), they are clearly visible for the velocity up to approximately 1 eV in Fig. 13 for low angles.

As already observed throughout this paper, a minimum in the DOS caused by a Dirac point does not necessarily imply a maximum in the velocity. This is further confirmed with this energy-dependent renormalized velocity curve. Changing from 90° to 0°, a maximum in the velocity can become a minimum at the position of the additional Dirac cones. In other words, the Dirac cones away from the CNP induce a local maximum of the velocity in the direction parallel to the barrier and a minimum in the direction perpendicular to the barrier. Finally, the energy-dependent oscillations in the velocity are more pronounced with increasing values of U (not shown here).

VI. EFFECT OF DISORDER

All the potential barriers considered so far were ideal and displayed a perfect periodicity, keeping therefore the charge carriers in the ballistic regime. The absence of random disorder precludes quantum interference phenomena, such as weak and strong localization effects. Therefore, to observe the transport signatures from this paper, experiments should aim at minimizing any form of extrinsic disorder (adatoms, vacancies, trapped screened charged impurities) that may lead to strong scattering. In addition, the barriers themselves should be free of disorder and atomically perfect. This situation is obviously rather far from real experimental conditions. Existing literature
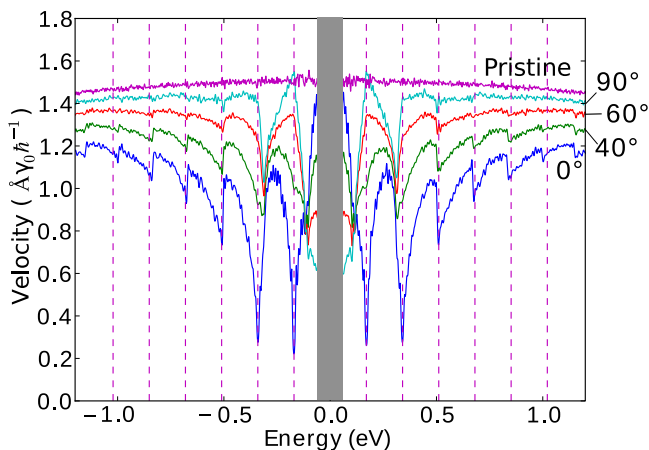

FIG. 13. (Color online) Energy dependence of the velocity at different angles, for ZSLs. The first curve on the top is for pristine graphene. The direction perpendicular to the barrier is taken as 0° reference. From top to bottom the angles are 90° ($v_\parallel$), 60°, 40°, and 0° ($v_\perp$). The vertical dashed lines represent the position of the new Dirac points generated by the SLs as given by Eq. (4). The potential applied is $U = 0.52$ eV with a period of $L = 10$ nm ($W = L/2$). The area around the CNP is shaded because the results are numerically too unstable there.
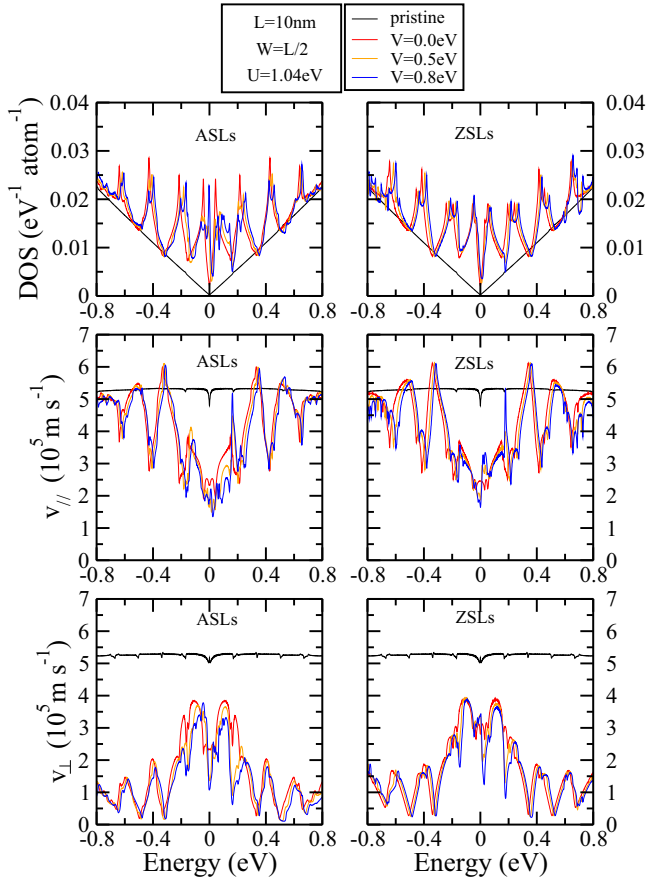
FIG. 14. (Color online) Density of states and velocities for ASLs and ZSLs ($L = 10$ nm, $W = L/2$, $U = 1.04$ eV) without ($V = 0$ eV) and with Anderson disorder ($V = 0.5$ and 0.8 eV).

gives guidance on which features should remain robust and which features might disappear if such disorder becomes too strong. More specifically, for uncorrelated white-noise disorder on the barriers, a perpendicular incident angle keeps a robust transmission [49], suggesting that the associated transport features are reliable, while the transmission is strongly reduced when the incident angle is increased. The system should therefore be kept as clean as possible to observe parallel conductivity features (the perpendicular case being less sensitive). To counter the detrimental effect of white-noise disorder on the transmission, a long-range correlation between the potential barriers may be used [24,50].

The systematic study of the effect of disorder on the electronic transport in graphene 1D SLs is out of the scope of this article. However, selected prospective simulations of disordered graphene 1D SLs are presented in Fig. 14. The upper panels compare the effect of Anderson (white-noise) disorder on the DOS of both ASLs (left) and ZSLs (right). Anderson disorder is introduced by randomly varying the onsite potentials of all atomic sites with a value of $\delta \varepsilon_{p_z} \in [-V/2, +V/2]$. The existence and the position of the new Dirac points remains noticeably robust, up to $V = 0.8$ eV. Equation (4) can still be used to estimate their position. However, disorder induces a splitting in the secondary VHS for the ASLs, while this splitting already exists in the absence

of disorder for ZSLs. Smoothed curves and VHS peaks may be expected by averaging over a manifold of disorder configurations. This makes it very difficult to experimentally differentiate between ASLs and ZSLs, based on the DOS. In Fig. 14, both parallel (central panels) and perpendicular (lower panels) velocities are plotted for ASLs (left panels) and ZSLs (right panels). The black curves give the velocity for pristine graphene, in absence of SLs and Anderson disorder. Applying the Anderson disorder (yellow and blue curves) on top of the clean SL (red curve) does not change much the behavior of both velocity directions above ± 0.3 eV, which is as expected due to the selected V values. Nevertheless, the qualitative features (maxima and minima) remain globally robust even for low energies. At zero energy, a drop by a factor of two for $V = 0.8$ eV is observed for both velocities for the ASL case. For the ZSLs case, the changes in velocity at low energy are smaller, with the perpendicular features even more robust, in agreement with the above statements based on literature. Nevertheless, for both SL orientations, a large drop (increase) of the perpendicular (parallel) velocity appears around 0.2 eV, respectively. Further calculations would be required to complete this picture, but these preliminary velocity and DOS calculations indicate that ZSLs are more robust to the detrimental effect of Anderson disorder than ASLs.

VII. CONCLUSION

The effect of the 1D SL orientation with respect to the graphene crystal is taken into account in this study of velocity renormalization and Dirac cone multiplication. Important differences were highlighted, like the presence of new cones at the CNP for zigzag SLs and the opening of gaps for armchair SLs. A specific effect induced by the SL alignment, absent in the literature, was found in the velocity renormalization for the direction perpendicular to the 1D potential. This renormalization occurs in ASLs, in general, and in ZSLs when the barriers are asymmetric. On the other hand, the velocity in the direction parallel to the 1D potential behaves similarly to what is predicted in the literature, although the position of the minima can be modulated by the type of SLs or the parameters used. The asymmetry of the SLs was shown to have a strong impact on the velocity. In particular, it can break the initial symmetry between the forward and backward momentum direction with respect to the Dirac cone symmetry for the velocity in the perpendicular direction for ASLs and parallel direction for ZSLs. This breaking of the symmetry can be interpreted by a rotation and deformation of the Dirac cone(s), leading to strong modifications in the associated velocities. By studying the angle dependence of the velocity through the barrier, the smooth transition between the parallel and perpendicular direction is understood. The calculated gaps in ASLs are very small. More advanced theoretical frameworks, such as *ab initio* simulations, are required to correctly assess their amplitude. Further studies may focus on systems with mixed chiral orientation different than the pure armchair or zigzag orientations reproducing certain experimental conditions. Nevertheless, much improved control of edge geometry (using a bottom-up approach for chemical synthesis [51–54]) make the present systems promising for electron collimation experiments.

APPENDIX: NUMERICAL INSTABILITY AT THE CHARGE NEUTRAL POINT

Numerical instabilities make an accurate calculation of the velocity at the CNP difficult. In the following, we show why and how numerical instabilities appears at the CNP. This feature is illustrated within the Kubo-Greenwood approach, which we further describe here.

The Kubo-Greenwood technique was originally developed to compute the conductivity from the quantum-mechanical point of view [35,41–43] and gives information on both the quantum and the semi-classical transport. The energy-dependent carrier velocities in the ballistic regime can also be investigated using this formalism. The formalism is based on the propagation of a wave packet throughout the material, described by the diffusion coefficient D defined as

$$D(t) = \frac{\partial}{\partial t}\Delta R^2(t) = \frac{\partial}{\partial t}\Delta X^2(t) + \frac{\partial}{\partial t}\Delta Y^2(t), \quad \text{(A1)}$$

where $\Delta R^2(t)$ is the mean quadratic spreading of the wave packet. $\Delta X^2(t)$ and $\Delta Y^2(t)$ are the mean quadratic spreadings in the x and y direction, respectively. The behavior of D with time indicates the transport regime in which the wave packet resides [40]. If the diffusion coefficient increases linearly with time, the electrons are not scattered and move freely in the material (ballistic regime). When this coefficient saturates to a certain value ($D^{\max}$), the electrons have experienced sufficient scattering to reach the diffusive regime. A further increase or decrease of the coefficient indicates the onset of (anti-)localization [35,43], rooting in quantum localization corrections. The diffusion coefficient D depends on the mean quadratic spreading of the wave packet as described

in Eq. (A1), while the spreading in a given direction (say, x) is given by

$$\Delta X^2(t) = \langle|\hat{X}(t) - \hat{X}(0)|^2\rangle_E$$
$$= \frac{\text{Tr}[(\hat{X}(t) - \hat{X}(0))^*\delta(E - \hat{H})(\hat{X}(t) - \hat{X}(0))]}{\text{Tr}[\delta(E - \hat{H})]},$$
$$\text{(A2)}$$

where the operator $\hat{X}(t)$ is the position operator in the Heisenberg picture. The numerator, and the denominator (corresponding to the DOS), are computed separately, with the same Lanczos algorithm using continued fractions. To reduce the computational cost, the trace is replaced by an average of random phase states obtained by adding a random phase factor to the wave function at each orbital of the system. Averaging over about ten random phase states is usually enough to reach a satisfactory convergence ($<1\%$ of variations in the quantities of interest).

The velocity in the ballistic regime can be extracted from the mean quadratic expansion as

$$\Delta X^2(t) = v_x^2 t^2 \Rightarrow v_x = \frac{\sqrt{\Delta X^2(t)}}{t}. \quad \text{(A3)}$$

In pristine graphene, at the CNP, both the numerator and the denominator of $\Delta X^2(t)$ [Eq. (A2)] tend to zero. The denominator being the graphene DOS at the Dirac point means that this term obviously tends to zero. From simple physical considerations using Eq. (A3), one can show that the numerator of $\Delta X^2(t)$ also tends to zero. Indeed, a finite value of velocity implies a finite value of $\Delta X^2(t)$. Since the denominator of $\Delta X^2(t)$ tends to zero in Eq. (A2), a finite spreading can only exist if the numerator tends to zero too. Mathematically, using the concept of limits, this is no problem. From a numerical point of view, using floating point arithmetics, the division of two very small numbers generates large errors, explaining the aforementioned instability. A similar problem can arise when calculating the energy-dependent velocity with a direct diagonalization approach. However, in that case, the accuracy is much more controlled and the results can be improved by using denser k-point meshes in the Brillouin zone. The Kubo-Greenwood approach was nevertheless helpful in this article to compute the energy-dependent velocity at any intermediate angles as shown in Fig. 13.

---

[1] K. S. Novoselov, A. K. Geim, S. V. Morozov, D. Jiang, Y. Zhang, S. V. Dubonos, I. V. Grigorieva, and A. A. Firsov, Science **306**, 666 (2004).

[2] K. Novoselov, Rev. Mod. Phys. **83**, 837 (2011).

[3] A. K. Geim and K. S. Novoselov, Nat. Mater. **6**, 183 (2007).

[4] M. Katsnelson, K. Novoselov, and A. Geim, Nat. Phys. **2**, 620 (2006).

[5] K. Novoselov, A. K. Geim, S. Morozov, D. Jiang, M. K. I. Grigorieva, S. Dubonos, and A. Firsov, Nature **438**, 197 (2005).

[6] M. C. Lemme, Solid State Phenom. **156**, 499 (2010).

[7] H. Yamaguchi, G. Eda, C. Mattevi, H. Kim, and M. Chhowalla, ACS Nano **4**, 524 (2010).

[8] Y. Wu, Y.-M. Lin, A. Bol, K. Jenkins, F. Xia, D. Farmer, Y. Zhu, and P. Avouris, Nature **472**, 74 (2011).

[9] T. Palacios, Nat. Nanotechnol. **6**, 464 (2011).

[10] F. Schwierz, Nat. Nanotechnol. **5**, 487 (2010).

[11] C. Park, L. Yang, Y. Son, M. L. Cohen, and S. G. Louie, Nat. Phys. **4**, 213 (2008).

[12] C.-H. Park, L. Yang, Y.-W. Son, M. L. Cohen, and S. G. Louie, Phys. Rev. Lett. **101**, 126804 (2008).

[13] P. Burset, A. L. Yeyati, L. Brey, and H. A. Fertig, Phys. Rev. B **83**, 195434 (2011).

[14] A. L. Vázquez de Parga, F. Calleja, B. Borca, M. C. G. Passeggi, J. J. Hinarejos, F. Guinea, and R. Miranda, Phys. Rev. Lett. **100**, 056807 (2008).

[15] I. Pletikosić, M. Kralj, P. Pervan, R. Brako, J. Coraux, A. T. N'Diaye, C. Busse, and T. Michely, Phys. Rev. Lett. **102**, 056808 (2009).

[16] R. P. Tiwari and D. Stroud, Phys. Rev. B **79**, 205435 (2009).

[17] F. Guinea and T. Low, Philos. Trans. R. Soc., A **368**, 5391 (2010).

[18] T. G. Pedersen, C. Flindt, J. Pedersen, N. A. Mortensen, A.-P. Jauho, and K. Pedersen, Phys. Rev. Lett. **100**, 136804 (2008).

[19] J. A. Fürst, J. G. Pedersen, C. Flindt, N. A. Mortensen, M. Brandbyge, T. G. Pedersen, and A.-P. Jauho, New J. Phys. **11**, 095020 (2009).

[20] A. J. M. Giesbers, E. C. Peters, M. Burghard, and K. Kern, Phys. Rev. B **86**, 045445 (2012).

[21] J. Eroms and D. Weiss, New J. Phys. **11**, 095021 (2009).

[22] J. G. Pedersen, A. W. Cummings, and S. Roche, Phys. Rev. B **89**, 165401 (2014).

[23] C.-H. Park, Y.-W. Son, L. Yang, M. L. Cohen, and S. G. Louie, Nano Lett. **8**, 2920 (2008).

[24] M. Barbier, P. Vasilopoulos, and F. M. Peeters, Philos. Trans. R. Soc., A **368**, 5499 (2010).

[25] M. Yankowitz, J. Xue, D. Cormode, J. Sanchez-Yamagishi, K. Watanabe, T. Taniguchi, P. Jarillo-Herrero, P. Jacquod, and B. Leroy, Nat. Phys. **8**, 382 (2012).

[26] L. Ponomarenko, R. Gorbachev, G. Yu, D. Elias, R. Jalil, A. Patel, A. Mishchenko, A. Mayorov, C. Woods, J. Wallbank *et al.*, Nature (London) **497**, 594 (2013).

[27] C. Dean, L. Wang, P. Maher, C. Forsythe, F. Ghahari, Y. Gao, J. Katoch, M. Ishigami, P. Moon, M. Koshino *et al.*, Nature (London) **497**, 598 (2013).

[28] B. Hunt, J. Sanchez-Yamagishi, A. Young, M. Yankowitz, B. LeRoy, K. Watanabe, T. Taniguchi, P. Moon, M. Koshino, P. Jarillo-Herrero *et al.*, Science **340**, 1427 (2013).

[29] W. Yang, G. Chen, Z. Shi, C.-C. Liu, L. Zhang, G. Xie, M. Cheng, D. Wang, R. Yang, D. Shi *et al.*, Nat. Mater. **12**, 792 (2013).

[30] H. Yan, Z.-D. Chu, W. Yan, M. Liu, L. Meng, M. Yang, Y. Fan, J. Wang, R.-F. Dou, Y. Zhang *et al.*, Phys. Rev. B **87**, 075405 (2013).

[31] S. Dubey, V. Singh, A. K. Bhat, P. Parikh, S. Grover, R. Sensarma, V. Tripathi, K. Sengupta, and M. M. Deshmukh, Nano Lett. **13**, 3990 (2013).

[32] M. Barbier, P. Vasilopoulos, and F. M. Peeters, Phys. Rev. B **81**, 075438 (2010).

[33] J. H. Ho, Y. H. Chiu, S. J. Tsai, and M. F. Lin, Phys. Rev. B **79**, 115427 (2009).

[34] J.-K. Lee, S. Yamazaki, H. Yun, J. Park, G. P. Kennedy, G.-T. Kim, O. Pietzsch, R. Wiesendanger, S. Lee, S. Hong *et al.*, Nano Lett. **13**, 3494 (2013).

[35] N. Leconte, A. Lherbier, F. Varchon, P. Ordejon, S. Roche, and J.-C. Charlier, Phys. Rev. B **84**, 235420 (2011).

[36] K. Nakada, M. Fujita, G. Dresselhaus, and M. S. Dresselhaus, Phys. Rev. B **54**, 17954 (1996).

[37] Y.-W. Son, M. L. Cohen, and S. G. Louie, Phys. Rev. Lett. **97**, 216803 (2006).

[38] Q. Yu, L. A. Jauregui, W. Wu, R. Colby, J. Tian, Z. Su, H. Cao, Z. Liu, D. Pandey, D. Wei *et al.*, Nat. Mater. **10**, 443 (2011).

[39] X. Lei-Jiang, Y. Fang, Z. Hai-Qing, and S. Lian-Feng, Chin. Phys. B **24**, 036802 (2015).

[40] A. Lherbier, Ph.D. thesis, Universite Joseph-Fourier - Grenoble I, 2008.

[41] S. Roche and D. Mayou, Phys. Rev. Lett. **79**, 2518 (1997).

[42] S. Roche, Phys. Rev. B **59**, 2284 (1999).

[43] S. Roche, N. Leconte, F. Ortmann, A. Lherbier, D. Soriano, and J.-C. Charlier, Solid State Commun. **152**, 1404 (2012).

[44] Z. Fan, A. Uppstu, T. Siro, and A. Harju, Comput. Phys. Commun. **185**, 28 (2014).

[45] T. M. Radchenko, A. A. Shylau, and I. V. Zozoulenko, Phys. Rev. B **86**, 035418 (2012).

[46] G. Trambly de Laissardière and D. Mayou, Mod. Phys. Lett. B **25**, 1019 (2011).

[47] R. Haydock, Comput. Phys. Commun. **20**, 11 (1980).

[48] J. Chae, S. Jung, A. F. Young, C. R. Dean, L. Wang, Y. Gao, K. Watanabe, T. Taniguchi, J. Hone, K. L. Shepard *et al.*, Phys. Rev. Lett. **109**, 116802 (2012).

[49] N. Abedpour, A. Esmailpour, R. Asgari, and M. R. R. Tabar, Phys. Rev. B **79**, 165412 (2009).

[50] A. Esmailpour, H. Meshkin, and R. Asgari, Solid State Commun. **152**, 1896 (2012).

[51] J. Campos-Delgado, J. M. Romo-Herrera, X. Jia, D. A. Cullen, H. Muramatsu, Y. A. Kim, T. Hayashi, Z. Ren, D. J. Smith, Y. Okuno *et al.*, Nano Lett. **8**, 2773 (2008).

[52] M. Sprinkle, M. Ruan, Y. Hu, J. Hankinson, M. Rubio-Roy, B. Zhang, X. Wu, C. Berger, and W. A. De Heer, Nat. Nanotechnol. **5**, 727 (2010).

[53] J. Cai, P. Ruffieux, R. Jaafar, M. Bieri, T. Braun, S. Blankenburg, M. Muoth, A. P. Seitsonen, M. Saleh, X. Feng *et al.*, Nature (London) **466**, 470 (2010).

[54] T. Kato and R. Hatakeyama, Nat. Nanotechnol. **7**, 651 (2012).